

1. Introduction

IAC-20-C1,4,8,x55549

LOW-THRUST TRAJECTORY OPTIMIZATION FOR CUBESAT LUNAR MISSION: HORYU-VI

Omer Burak Iskender^{a,*}, Keck Voon Ling^c, Mengu Cho^{b,c}, Sangkyun Kim^b, and Necmi Cihan Orger^b

^a*Nanyang Technological University, Singapore, iske0001@e.ntu.edu.sg*

^b*Kyushu Institute of Technology, Kitakyushu, Japan*

^c*Nanyang Technological University, Singapore*

^{*}*Corresponding author*

Abstract

This paper presents a low-thrust trajectory optimization strategy to achieve a near-circular lunar orbit for a CubeSat injected into a lunar flyby trajectory. The 12U CubeSat HORYU-VI is equipped with four hall-effect thrusters and designed as a secondary payload on NASA's Space Launch System under the Artemis program. Upon release, the spacecraft gains sufficient energy to escape the Earth–Moon system after a lunar flyby. The proposed trajectory is decomposed into three phases: (1) pre-flyby deceleration to avoid heliocentric escape, (2) lunar gravitational capture, and (3) orbit circularization to the science orbit. For each phase, an impulsive-burn solution is first computed as an initial guess, which is then refined through finite-burn optimization using Sequential Quadratic Programming (SQP). The dynamical model incorporates Earth–Moon–Sun–Jupiter gravitational interactions and a high-fidelity lunar gravity field. All trajectories are independently verified with NASA's General Mission Analysis Tool (GMAT). Results demonstrate that HORYU-VI achieves lunar capture within 200 days, establishes a stable science orbit at 280 days, and can spiral down to a near-circular 100 km orbit by 450 days, using a total ΔV of 710 m/s, well within the capability of the electric propulsion system.

Keywords: Electric Propulsion, Trajectory Optimization, Low Thrust, CubeSat, Lunar Mission, HORYU-VI

Published at the 71st International Astronautical Congress (IAC 2020), The CyberSpace Edition, 12–14 October 2020. Paper ID: IAC-20-C1,4,8,x55549.

1. INTRODUCTION

CubeSat platforms have rapidly expanded their reach from Low Earth Orbit (LEO) to cis-lunar and interplanetary space, offering cost-effective spacecraft for scientific and technological objectives.^{2,6,10,14,24} Lunar science has emerged as a primary focus for next-generation CubeSat missions.

The HORYU-VI mission is an international CubeSat initiative to investigate the lunar dust environment through multi-epoch imaging of the Lunar Horizon Glow (LHG).²² The project is a collaboration among Kyushu Institute of Technology (Japan), Nanyang Technological University (Singapore), Sapienza University of Rome (Italy), California Polytechnic State University (USA), University of Colorado Boulder (USA), and Alienia Pte. Ltd. (Singapore). The 12U CubeSat platform carries dedicated imaging instruments for LHG observations from a low-altitude lunar orbit.

The LHG (an anomalous brightness above the lu-

nar terminator exceeding the Coronal Zodiaca Light (CZL) baseline) was first observed during the Apollo era.^{4,17,18,26} Lunar dust poses hazards to both crewed missions (respiratory risks, contamination, long-term health effects)^{7,11,13,15} and robotic systems (optical degradation, thermal property alterations, electrical discharges).^{8,20,21} Characterizing the near-surface dust population from orbit remains an open challenge in lunar science.^{1,3,5,9,27}

Low-thrust propulsion (where each thruster head produces sub-millinewton thrust levels, resulting in milli- g or lower acceleration) is fundamentally different from the high-thrust impulsive maneuvers used in conventional direct lunar transfers. For CubeSats, low thrust typically means less than 1 mN per thruster, with burn durations on the order of months. The enabling technology is electric propulsion (EP), which uses electrical power to accelerate a propellant and thereby impart velocity changes with high fuel efficiency. EP offers three principal advantages over chemical systems: high specific impulse (and hence low propellant consumption), low hardware cost, and highly controllable, precise thrust vectoring. The technology traces back to the first space-qualified ion engines in 1964, followed by pulsed plasma thrusters, and

2. Trajectory Options

Table 1. Lunar transfer methods with typical duration and representative missions.²³

Transfer Type	Typical Duration	Benefits	Example
Direct, conventional	3–6 days	Well known, quick	Apollo, LRO
Direct, staging	2–10 weeks	Quick, many launch days	Clementine, CH-1
Direct to lunar L1	1–5 weeks	Staging at L1	Few to date
Low-thrust	Many months	Low fuel, many launch days	SMART-1
Low-energy	2.5–4 months	Low fuel, many launch days	Hiten, GRAIL, ARTEMIS

LRO: Lunar Reconnaissance Orbiter; CH-1: Chandrayaan-1; SMART-1: Small Missions for Advanced Research in Technology.

the Hall-effect thrusters that are now the most common EP devices for small satellites.

This paper addresses the trajectory design challenge for HORYU-VI. The launch opportunity was envisioned as a secondary payload on NASA’s Space Launch System (SLS) under the Artemis program. Upon separation, the CubeSat enters a high-eccentricity orbit ($e = 0.9667$) with sufficient energy for lunar flyby and subsequent heliocentric escape if left uncontrolled. Converting this trajectory into a stable lunar orbit requires precise multi-phase low-thrust maneuvers within the severe propulsion constraints of a CubeSat platform.

2. TRAJECTORY OPTIONS

Table 1 summarizes established lunar transfer methods.²³ The SMART-1 mission pioneered low-thrust cislunar transfers using a Hall-effect thruster, requiring ~ 14 months to reach lunar orbit from GTO.²⁵ Its four-phase approach (GTO spiral-out, further orbit raising, lunar capture via Pontryagin’s Maximum Principle, and circularization) provides the operational heritage for HORYU-VI. The present work adopts a similar phased decomposition but differs in that the initial orbit is a high-energy flyby trajectory rather than GTO.

3. MISSION ARCHITECTURE

The HORYU-VI spacecraft is a 12U CubeSat (dry mass 9 kg, propellant 3 kg, wet mass 12 kg) equipped with four hall-effect thrusters ($I_{sp} = 1000$ s) providing a combined nominal thrust of 1.2 mN (1.08 mN effective, assuming 10% inefficiency), and a total ΔV capability of 930 m/s. Table 2 presents the spacecraft state at separation from the launch vehicle. Fig. 1 shows the CAD model.

3.1 Uncontrolled trajectory

Ballistic propagation of the initial state reveals that the spacecraft performs an uncontrolled lunar flyby at approximately 1300 km altitude and subsequently escapes into a heliocentric orbit after ~ 4.2 days (Figs. 2–3). To establish a stable lunar orbit, the mission trajectory is divided into four segments:

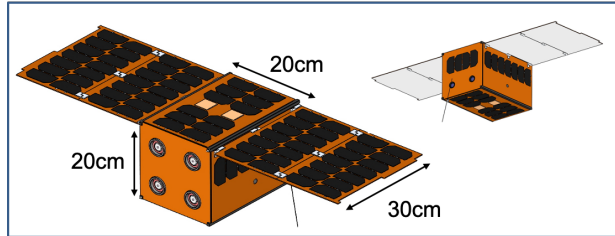


Fig. 1. CAD design of HORYU-VI CubeSat.

Table 2. Spacecraft state at separation from the launch vehicle.^{16,19}

Parameter	Value	Unit	Parameter	Value	Unit
X	-15015.4	km	SMA	205954.8	km
Y	-23569	km	Ecc	0.9667	
Z	2241.505	km	Inc	28.6065	deg
VX	-0.48554	km/s	RAAN	65.9569	deg
VY	-5.04876	km/s	AoP	47.9162	deg
VZ	-0.87999	km/s	TA	122.4711	deg
Epoch	15 December 2017				

Segment 0 – Detumbling and commissioning (~ 2 hours): Immediately after separation, the spacecraft detumbles and establishes the communication network. This preliminary segment must complete before propulsive maneuvers can begin.

Phase 1 – Pre-flyby deceleration: Anti-velocity (retrograde) thrust is applied over approximately 2 days to reduce the spacecraft energy below the lunar escape threshold.

Phase 2 – Lunar capture: The spacecraft is transitioned from Earth–Moon transfer to a highly eccentric ($e \approx 0.7$) lunar orbit with a semi-major axis $a \leq 32,000$ km through optimized thrust sequences over multiple perilune passages.

Phase 3 – Orbit circularization: Retrograde finite burns over 400 successive perilune passages reduce eccentricity from $e \approx 0.7$ to near-circular over ~ 270 days,

3.2 Reference frames

achieving the 100 km science orbit.

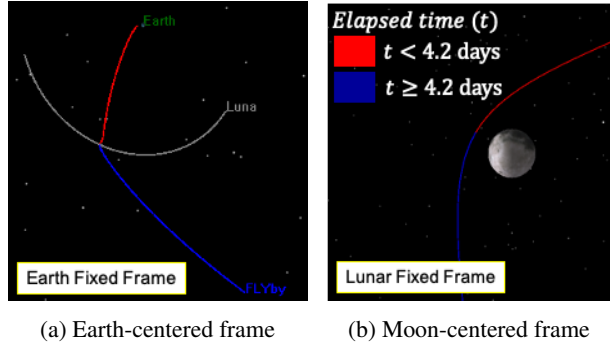


Fig. 2. Trajectory without actuation.

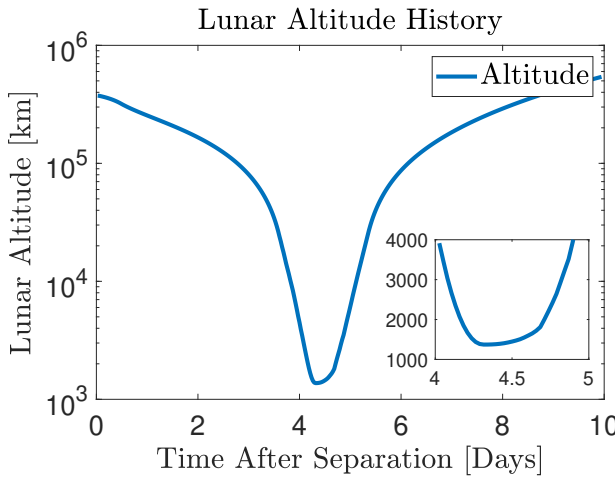


Fig. 3. Lunar altitude history without actuation.

3.2 Reference frames

The trajectory analysis employs three coordinate frames:

Earth-Centred Inertial (ECI): The primary frame for trajectory propagation. The origin is at the Earth's center of mass, with the *X*-axis directed toward the vernal equinox at the J2000 epoch and the *Z*-axis toward the celestial north pole. The axes are non-rotating (inertially fixed). The equations of motion (Eq. (1)) and the GMAT verification are formulated in this frame.

Earth-Centred Earth-Fixed (ECEF): The origin coincides with ECI but the axes rotate with the Earth at sidereal rate. The *X*-axis passes through the Greenwich meridian. This frame is used for ground-station visibility calculations and launch geometry, but is *not* used for orbit propagation.

Moon-Centred Inertial (MCI): The origin is at the Moon's center of mass, with axes parallel to the ECI

J2000 frame. Lunar orbital elements, altitude histories, and the capture/circularization trajectory plots (Figs. 2b, 7) are presented in this frame. Lunar altitude is computed in a selenocentric body-fixed frame that rotates with the Moon.

3.3 Dynamical model

The equations of motion are formulated in the ECI frame incorporating n-body gravitational dynamics:

$$\ddot{\mathbf{r}} = -\frac{\mu_{\oplus}}{r^3} \mathbf{r} - \mu_M \left(\frac{\mathbf{r} - \mathbf{r}_M}{|\mathbf{r} - \mathbf{r}_M|^3} + \frac{\mathbf{r}_M}{r_M^3} \right) + \mathbf{a}_{3rd} + \frac{\mathbf{F}_{thrust}}{m} \quad (1)$$

where μ_{\oplus} and μ_M are the gravitational parameters of Earth and Moon, $\mathbf{r}_M(t)$ is the lunar position from JPL ephemerides, and \mathbf{a}_{3rd} accounts for Sun and Jupiter perturbations. Near the Moon, the GGLP1500D gravity field (degree and order 1500) replaces the point-mass lunar model.

The combined thrust from all active thrusters is bounded by:

$$\|\mathbf{F}_{total}\| \leq 1.2 \text{ mN} \quad (2)$$

with a 10% inefficiency margin applied in the GMAT simulation (thrust scale factor 0.9), yielding an effective thrust of 1.08 mN. The exhaust velocity is $v_e = g_0 I_{sp} \approx 9.81 \text{ km/s}$.

4. TRAJECTORY OPTIMIZATION

4.1 Problem formulation

A conventional approach to trajectory design is to solve a targeting problem using differential corrections, which satisfies endpoint constraints but does not optimize the trajectory. Instead, this work optimizes the low-thrust trajectory with a time-varying thrust profile using nonlinear programming. While commercial solvers such as SNOPT and IPOPT are available, the optimization requires high-fidelity force models to accurately capture flight dynamics over multi-month transfer durations. NASA's General Mission Analysis Tool (GMAT)¹² provides out-of-the-box force models and numerical propagators at the highest available fidelity, and its built-in YUKON optimizer (a nonlinear programming solver based on Sequential Quadratic Programming (SQP)) was therefore adopted. To achieve the best orbit propagation accuracy, two separate thruster models are employed: an Earth-centered thruster whose thrust direction is defined in the Earth VNB (velocity–normal–binormal) frame for Phases 1–2 (when the spacecraft is in Earth's close proximity), and a Moon-centered thruster whose direction is defined in the lunar VNB frame for capture and circularization (during lunar close proximity). This hybrid formulation ensures that the central body providing the dominant gravitational field is used for propagation in

4.1 Problem formulation

each phase, avoiding numerical errors from computing small perturbation differences relative to a distant primary. The design variables for the YUKON optimization are the three-dimensional thrust direction vectors for the transition-burn and capture-burn phases ($\hat{\mathbf{d}}_{\oplus}, \hat{\mathbf{d}}_M \in \mathbb{R}^3$), the transition-burn duration Δt_{burn} , and the coast duration between transition and capture Δt_{coast} , yielding eight design variables in total. The constrained optimization problem is formulated as:

$$\begin{aligned}
 & \text{find} && \text{feasible trajectory} \\
 & \hat{\mathbf{d}}_{\oplus}, \hat{\mathbf{d}}_M, \Delta t_{\text{burn}}, \Delta t_{\text{coast}} && \\
 & \text{subject to} && \dot{\mathbf{r}} = \mathbf{v}, \quad \dot{\mathbf{v}} = \mathbf{a}_{\text{grav}} + \frac{\mathbf{F}_{\text{thrust}}}{m} \\
 & && 0 \leq \|\mathbf{F}_{\text{thrust}}\| \leq F_{\text{max}} \\
 & && r_{\text{peri}} \geq 6,000 \text{ km} \\
 & && C_3 \leq -0.11 \text{ km}^2/\text{s}^2
 \end{aligned} \tag{3}$$

where r_{peri} is the periapsis distance from the Moon's center and C_3 is the characteristic energy with respect to the Moon at the end of the capture burn. The periapsis constraint ensures sufficient altitude to avoid surface impact, while the C_3 constraint guarantees gravitational capture (negative C_3 indicates an elliptical, bound orbit). The dynamical constraints follow Eq. (1) and the thrust bound from Eq. (2).

The choice of capture constraints was determined through a systematic trade study (Table 3), motivated by three distinct failure modes observed in our simulations:

1. *No feasible solution*: When low eccentricity constraints are enforced ($e \leq 0.4$), the optimizer cannot find a trajectory satisfying all constraints simultaneously.
2. *Escape*: The optimizer converges and constraints are satisfied, but the post-capture orbit is not stable (the CubeSat escapes from the Moon's gravitational attraction).
3. *Surface impact*: Constraints are satisfied and the Moon is the dominant gravitational attractor; however, the CubeSat crashes onto the lunar surface due to insufficient periapsis altitude.

Three constraint formulations were evaluated to address these failure modes: (i) eccentricity alone, (ii) eccentricity with a semi-major axis upper bound, and (iii) C_3 energy with a perilune distance (RMAG) lower bound. Constraining only eccentricity, the optimizer converges for all tested values; however, for $e \leq 0.6$ the orbit remains hyperbolic and the spacecraft escapes (failure mode 2), while $e = 0.7$ achieves capture but results

in a periapsis below the lunar surface (failure mode 3). Adding an SMA constraint prevents escape at all eccentricities, yet the periapsis altitude remains unsafely low. Only the C_3 -RMAG formulation ($C_3 \leq -0.11 \text{ km}^2/\text{s}^2$, $r_{\text{peri}} \geq 6000 \text{ km}$) simultaneously guarantees gravitational capture and a safe periapsis altitude. The final implementation adopts the C_3 -RMAG formulation for the YUKON optimizer, providing robust capture with adequate margin above the lunar surface.

4.1.1 Lunar capture (Phase 2)

The optimized capture sequence proceeds as follows: after the pre-flyby deceleration burn (Phase 1), the spacecraft coasts for approximately 77.5 days through multiple lunar passages. The YUKON optimizer then determines (i) the Earth-VNB thrust direction and duration (~ 10 days) for the transition burn, (ii) a coast interval (~ 33 days), and (iii) the Moon-VNB thrust direction for a capture burn that terminates at the next lunar periapsis. The capture burn switches the thruster reference frame from Earth-centered to Moon-centered VNB, aligning the thrust vector with the local velocity direction relative to the Moon for maximum deceleration efficiency. At the end of this sequence, the spacecraft achieves lunar capture with $C_3 \leq -0.11 \text{ km}^2/\text{s}^2$ and periapsis altitude above 6000 km.

4.1.2 Orbit circularization (Phase 3)

Following capture, the orbit is circularized through a deterministic sequence of 400 retrograde finite-burn arcs distributed over successive perilune passages. The Moon-centered thruster is set to a fixed retrograde direction ($\hat{\mathbf{d}}_M = [-1, 0, 0]^T$ in lunar VNB). Each cycle consists of a thrust arc spanning true anomaly $\nu = 240^\circ \rightarrow 130^\circ$ (passing through periapsis at $\nu = 0^\circ$), followed by a coast arc from $\nu = 130^\circ \rightarrow 240^\circ$ (passing through apoapsis at $\nu = 180^\circ$). By thrusting retrograde near periapsis, the apoapsis altitude is progressively lowered each orbit, reducing eccentricity toward near-circular. This burn-coast architecture concentrates the ΔV where gravitational losses are lowest and avoids continuous thrusting through the apoapsis region where retrograde thrust would inefficiently raise the periapsis.

A distinguishing feature of this problem is that the design variables extend beyond the conventional thrust direction vector. In most low-thrust trajectory optimization studies, the control is the thrust orientation profile and the transfer duration is either fixed or a single scalar parameter. Here, the CubeSat's limited thrust capability (1.2 mN) is insufficient to achieve lunar gravitational capture during a single flyby passage (even under continuous maximum retrograde thrust, the hyperbolic excess velocity cannot be reduced below the escape threshold within the brief perilune window). The spacecraft must therefore execute

4.2 Impulsive-burn approximation

Table 3. Constraint trade study for Phase 2 lunar capture. Three formulations are compared: eccentricity only, eccentricity with SMA bound, and C_3 energy with perilune distance (RMAG).

Value	Ecc constraint			Ecc + SMA constraint			C_3 + RMAG
	0.5	0.6	0.7	0.5	0.6	0.7	$-0.15 \text{ km}^2/\text{s}^2, 6000 \text{ km}$
Constraint satisfaction	Yes	Yes	Yes	Yes	Yes	Yes	Yes
Avoid escape	No	No	Yes	Yes	Yes	Yes	Yes
Avoid lunar crash	–	–	No	No	No	No	Yes

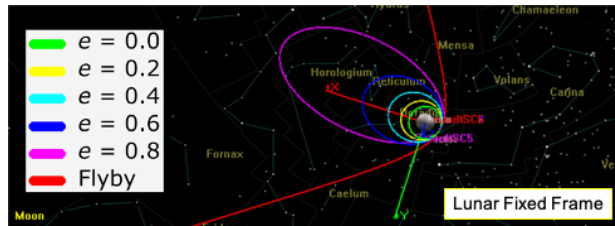


Fig. 4. Impulsive-burn trajectories in the Moon-centered frame.

multiple lunar passages, and the thrust-arc durations and coast intervals between successive encounters become essential decision variables alongside the thrust direction. This couples the inherently discrete question of *how many passages are required* with the continuous optimization of *when to thrust and when to coast*, substantially enlarging the design space compared to conventional single-arc formulations.

Because SQP is a local optimizer, the solution is critically dependent on the quality of the initial guess. The multi-passage trajectory structure introduces multiple local minima corresponding to qualitatively different flyby sequences and burn-arc placements. To identify viable starting points, a systematic heuristic parametric search was conducted: impulsive-burn solutions were generated across a grid of burn timings, coast durations, and passage counts, and the most promising candidates were used to warm-start the YUKON optimizer. This procedure required iterative manual refinement (a time-consuming process even under the idealized assumption of perfect initial state knowledge and navigation accuracy). The strong dependence on heuristic initialization motivates future work on hybrid global-local optimization frameworks, where metaheuristic algorithms (e.g., differential evolution or particle swarm optimization) would explore the design space broadly before handing off to SQP for local refinement.

Table 4. Impulsive-burn ΔV requirements.

Eccentricity	ΔV (m/s)
0	977.8
0.2	793.7
0.4	639.3
0.6	497.5
0.8	364.5

4.2 Impulsive-burn approximation

For each phase, impulsive-burn solutions are first computed to provide initial guesses and establish lower bounds on required ΔV . Table 4 and Fig. 4 show the ΔV requirements for different target eccentricities at lunar orbit insertion.

4.3 Finite-burn optimization results

Using the impulsive solutions as initial guesses, the YUKON-based finite-burn optimization is executed for the transition and lunar capture phases (Phases 1–2). The two-stage approach (where impulsive-burn solutions warm-start the optimizer) reduces the number of SQP iterations by an order of magnitude compared to cold-start initialization. Convergence typically requires 80–150 major iterations, with the lunar capture phase being the most computationally demanding due to sensitivity in perilune passage timing.

Table 5 summarizes the optimized trajectory. After the 2-hour detumbling, the pre-flyby burn and two capture maneuvers together require approximately 200 days of burns and cruising (Phases 1–2) to avoid the lunar flyby and achieve gravitational capture. The eccentricity is then progressively reduced by firing the thrusters in the anti-velocity direction before and after each perigee passage (Phase 3), as shown in the eccentricity evolution (Fig. 12). Within 280 days from separation, the spacecraft achieves a stable orbit suitable for initiating scientific observations of the lunar horizon glow. Continued circularization burns over an additional 170 days further reduce eccentricity, approaching a near-circular 100 km orbit by

5. Robustness Analysis

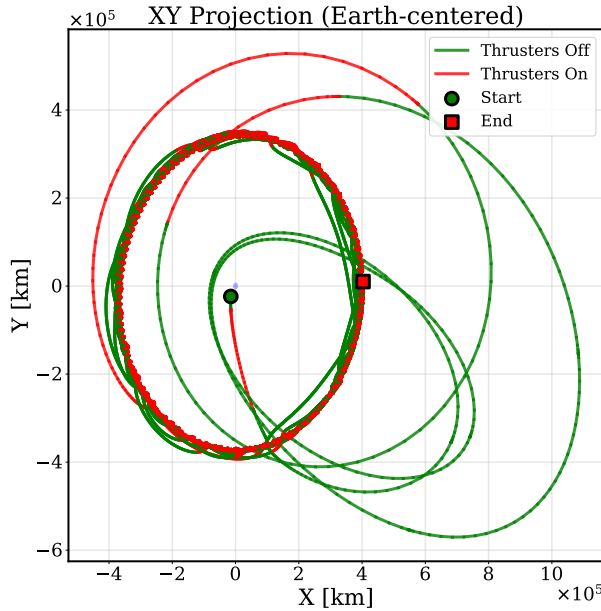


Fig. 5. Earth-centered XY projection of the optimized finite-burn trajectory (full resolution). Red: thrust active, green: coast.

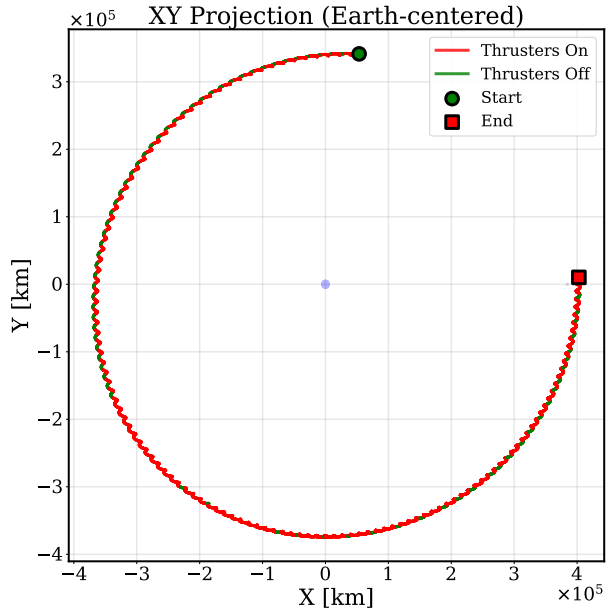


Fig. 6. Earth-centered XY projection of the optimized finite-burn trajectory (last 10,000 points). Red: thrust active, green: coast.

day 450 with 530 m/s ΔV expenditure during Phase 3 (Fig. 9). In total, the results demonstrate that HORYU-VI can establish a stable science orbit within 280 days and achieve near-circular geometry within 450 days using a total ΔV of 710 m/s (Fig. 9), which is achievable with the high-efficiency electric Hall-effect thrusters, requiring only ~ 1.2 kg of propellant from the 3 kg budget and leaving substantial margin for contingencies.

Figs. 5–7 show the optimized trajectory with burn arcs (red) and coast arcs (green) in both Earth-centered and Moon-centered reference frames. The color-coded representation clearly illustrates the distribution of thrust and coast phases throughout the mission, with the pre-flyby deceleration, transition burn, and lunar capture sequence visible in the Earth-centered view, while the Moon-centered view highlights the final capture.

The evolution of key orbital parameters throughout the mission is presented in Figs. 10–16. Fig. 10 shows the semi-major axis evolution with respect to the Moon, demonstrating the transition from hyperbolic approach (negative SMA) to the final captured elliptical orbit targeting $SMA \leq 10,000$ km. Fig. 12 presents the eccentricity history w.r.t. the Moon, showing the systematic reduction from the initial highly eccentric transfer orbit through the capture phase ($e = 0.7$) and subsequent circularization to near-circular geometry ($e < 0.05$). The dual-axis eccentricity plot (linear left, logarithmic right) enables visualization of the full eccentricity range from hyperbolic

(1000) through capture (0.7) to circular (0.1).

The inclination evolution (Fig. 13) reveals the spacecraft's orbital plane orientation relative to the Moon's equator, while Fig. 16 tracks the C_3 energy parameter w.r.t. the Moon (a critical indicator of gravitational capture that must remain below zero for bound lunar orbits). The transition from positive C_3 (hyperbolic, Moon-escape trajectory) to negative values (elliptical, gravitationally bound) marks successful lunar capture, with the constraint $C_3 \leq -0.11 \text{ km}^2/\text{s}^2$ ensuring deep capture and preventing re-escape. Distance evolution from Earth and Moon centers is shown in Figs. 17. The cumulative ΔV expenditure throughout the mission is presented in Fig. 9, showing the propellant consumption across all three mission phases with key milestones at capture (200 days), science orbit readiness (280 days), and near-circular orbit achievement (450 days).

5. ROBUSTNESS ANALYSIS

Preliminary sensitivity analysis indicates that initial condition uncertainties (particularly velocity errors at launch vehicle separation) represent the dominant risk factor. The high-eccentricity departure orbit creates a narrow corridor between lunar capture and heliocentric escape, making early autonomous thruster activation within hours of separation mission-critical. A comprehensive Monte Carlo robustness campaign is planned as future work to quantify mission success probability under re-

6. Conclusions

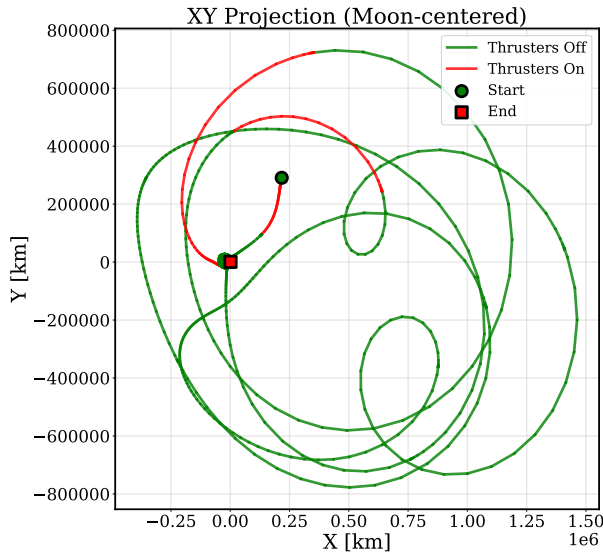


Fig. 7. Moon-centered XY projection of the optimized finite-burn trajectory (full resolution). Red: thrust active, green: coast.

Table 5. Optimized finite-burn trajectory summary with mission milestones.

Phase	Maneuver/Milestone	Epoch (days)	Duration (days)	ΔV (m/s)
1	Pre-flyby burn	0–2	2.0	17
	Transition burn	110–120	10.0	38
2	Lunar capture burn	150–175	25.0	125
	<i>Capture achieved</i>	200		
3	Orbit circularization	200–450	270.0	530
	<i>Science orbit stable</i>	280		
	<i>Near-circular orbit</i>	450		
Total active burn		307		710
Total mission (burn + coast)		450		

alistic multi-source uncertainties. Additionally, hybrid global-local optimization frameworks combining meta-heuristic design-space exploration with SQP local refinement are planned to overcome the strong initial guess sensitivity inherent in the multi-passage trajectory structure.

6. CONCLUSIONS

This paper has presented a low-thrust trajectory optimization strategy for the HORYU-VI 12U CubeSat lunar mission, with consideration of the requirements imposed by the Cube Quest Challenge¹⁹ and other mission subsystems, as well as self-imposed requirements. HORYU-VI is an international collaboration among Kyushu Institute of Technology (Japan), Nanyang Technological University (Singapore), Sapienza University of Rome (Italy), California Polytechnic State University (USA), University of Colorado Boulder (USA), and Alienia Pte. Ltd.

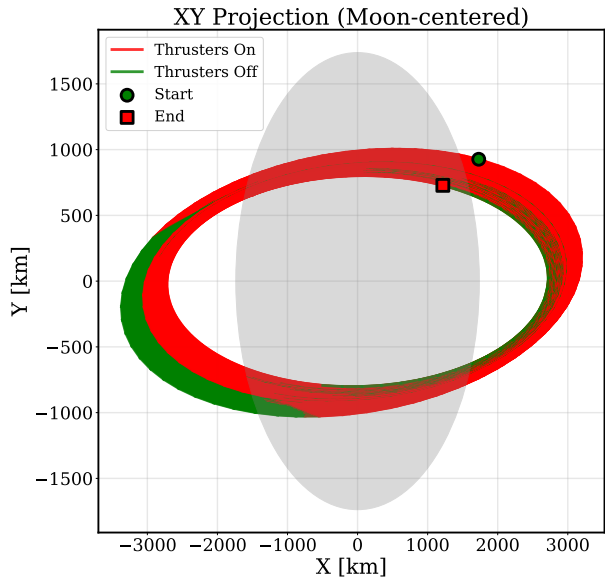


Fig. 8. Moon-centered XY projection of the optimized finite-burn trajectory (last 10,000 points). Red: thrust active, green: coast.

(Singapore), aimed at investigating the lunar dust charging environment through multi-epoch LHG imaging from lunar orbit.²²

The NASA GMAT design tool was heavily used for all simulations, and its built-in differential correction and

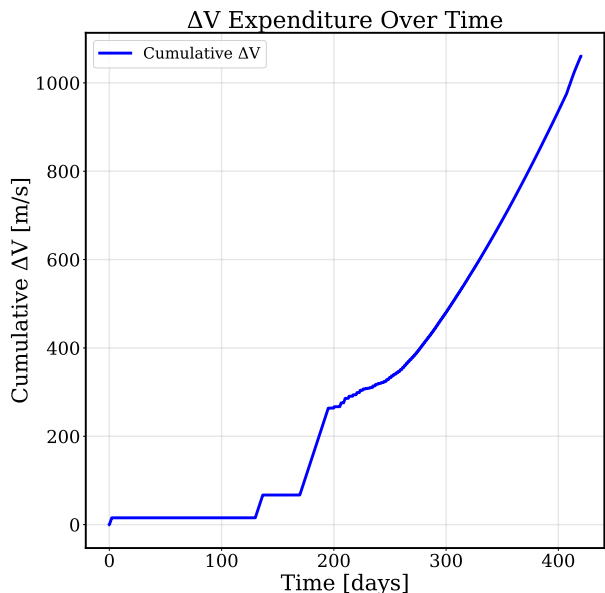


Fig. 9. Cumulative ΔV expenditure throughout the mission (full resolution).

support for the YUKON optimizer made it straightforward to perform all analysis. The three-phase trajectory architecture (pre-flyby deceleration, lunar capture, and orbit circularization) demonstrates that HORYU-VI achieves lunar capture within 200 days and establishes a stable science orbit by 280 days, with continued orbit refinement approaching near-circular geometry by 450 days, using a total ΔV of 710 m/s. The staged approach allows science operations to commence at 280 days while orbit optimization continues, balancing mission timeline constraints with propellant efficiency. The low ΔV requirement preserves significant propellant margin for trajectory adjustments and contingency operations. Sensitivity analysis identifies velocity errors at separation as the dominant risk factor.

Future work includes: adjusting the lunar Distant Retrograde Orbit (DRO) approach to allow a faster spiral-down process and reduce total thrust duration; investigating different spiral-down profiles to further reduce circularization burn time; a thorough analysis of the total fuel budget with specific attention to thrust error components, including errors in the thrust pointing control system, thrust magnitude, and solar radiation pressure modeling; development of global optimization techniques that can address various mass and propulsion system configurations to enhance mission adaptability; and a comprehensive Monte Carlo robustness campaign.

REFERENCES

- [1] MK Barker, E Mazarico, TP McClanahan, X Sun, GA Neumann, DE Smith, MT Zuber, and JW Head. Searching for lunar horizon glow with the lunar orbiter laser altimeter. *Journal of Geophysical Research: Planets*, 124(11):2728–2744, 2019.
- [2] BA Cohen, PO Hayne, BT Greenhagen, and DA Paige. Lunar flashlight: Exploration and science at the moon with a 6u cubesat. *AGUFM*, 2015:EP52B-07, 2015.
- [3] JE Colwell, S Batiste, M Horányi, S Robertson, and S Sture. Lunar surface: Dust dynamics and regolith mechanics. *Reviews of Geophysics*, 45(2), 2007.
- [4] DR Criswell. Horizon-glow and the motion of lunar dust. In *Photon and particle interactions with surfaces in space*, pages 545–556. Springer, 1973.
- [5] PD Feldman, DA Glenar, TJ Stubbs, KD Rutherford, GR Gladstone, PF Miles, TK Greathouse, DE Kauffmann, JW Parker, and SA Stern. Upper limits for a lunar dust exosphere from far-ultraviolet spectroscopy by lro/lamp. *Icarus*, 233:106–113, 2014.
- [6] DC Folta, N Bosanac, A Cox, and KC Howell. The lunar icecube mission design: Construction of feasible transfer trajectories with a constrained departure. In *AAS/AIAA Spaceflight Mechanics Meeting*, 2016.
- [7] JR Gaier. The effects of lunar dust on eva systems during the apollo missions: Nasa. Technical report, TM-2005-213610Cleveland: NASA Glenn Research Center, 2005.
- [8] JR Gaier. The effects of lunar dust on eva systems during the apollo missions. Technical report, National Aeronautics and Space Administration, 2007.
- [9] DA Glenar, TJ Stubbs, JE McCoy, and RR Vondrak. A reanalysis of the apollo light scattering observations, and implications for lunar exospheric dust. *Planetary and Space Science*, 59(14):1695–1707, 2011.
- [10] C Hardgrove, J DuBois, L Heffern, E Cisneros, J Bell, T Crain, R Starr, T Prettyman, I Lazbin, B Roebuck, et al. The lunar polar hydrogen mapper (lunah-map) mission. *Lunar Exploration Analysis Group*, 2015.
- [11] RS Harris. *Apollo experience report: Thermal design of Apollo lunar surface experiments package*. National Aeronautics and Space Administration, 1972.
- [12] SP Hughes. General mission analysis tool (gmat). 2016.
- [13] JT James, CW Lam, C Quan, WT Wallace, and L Taylor. Pulmonary toxicity of lunar highland dust. Technical report, SAE Technical Paper, 2009.
- [14] A Klesh, B Clement, C Colley, J Essmiller, D Forgette, J Krajewski, A Marinan, and T Martin-Mur. Marco: Early operations of the first cubesats to mars. In *Small Satellite Conference*, 2018.
- [15] D Linnarsson, J Carpenter, B Fubini, P Gerde, LL Karlsson, DJ Loftus, GK Prisk, U Staufer, EM Tranfield, and W van Westrenen. Toxicity of lunar dust. *Planetary and Space Science*, 74(1):57–71, 2012.
- [16] R Mathur. Low thrust trajectory design and optimization: Case study of a lunar cubesat mission. In *Proceedings of the 6th International Conference on Astrodynamics Tools and Techniques*, 2016.
- [17] JE McCoy. Photometric studies of light scattering above the lunar terminator from apollo solar corona

photography. In *Lunar and planetary science conference proceedings*, volume 7, pages 1087–1112, 1976.

[18] JE McCoy and DR Criswell. Evidence for a high altitude distribution of lunar dust. In *Lunar and planetary science conference proceedings*, volume 5, pages 2991–3005, 1974.

[19] NASA. Cube Quest Challenge. <https://www.nasa.gov/prizes-challenges-and-crowdsourcing/centennial-challenges/cube-quest-challenge/>, 2015. NASA Centennial Challenges, Space Technology Mission Directorate.

[20] BJ O'Brien. Review of measurements of dust movements on the moon during apollo. *Planetary and Space Science*, 59(14):1708–1726, 2011.

[21] BJ O'Brien. Paradigm shifts about dust on the moon: From apollo 11 to chang'e-4. *Planetary and Space Science*, 156:47–56, 2018.

[22] NC Örger, M Cho, OB Iskender, WS Lim, A Chandran, KV Ling, KH Holden, CL Chow, J Bellalardo, P Faure, et al. Horyu-vi: International cubesat mission to investigate lunar horizon glow. In *Proceedings of the 71st International Astronautical Congress (IAC)*, 2020. IAC-20,B4,2,7,x55547.

[23] J Parker and R Anderson. *Low-Energy Lunar Trajectory Design*. Jet Propulsion Laboratory, 01 2014.

[24] A Poghosyan and A Golkar. Cubesat evolution: Analyzing cubesat capabilities for conducting science missions. *Progress in Aerospace Sciences*, 88:59–83, 2017.

[25] GD Racca. Smart-1 from conception to moon impact. *Journal of Propulsion and Power*, 25(5):993–1002, 2009.

[26] JJ Rennilson and DR Criswell. Surveyor observations of lunar horizon-glow. *The moon*, 10(2):121–142, 1974.

[27] AB Severny, EI Terez, and AM Zvereva. The measurements of sky brightness on lunokhod-2. *The Moon*, 14(1):123–128, 1975.

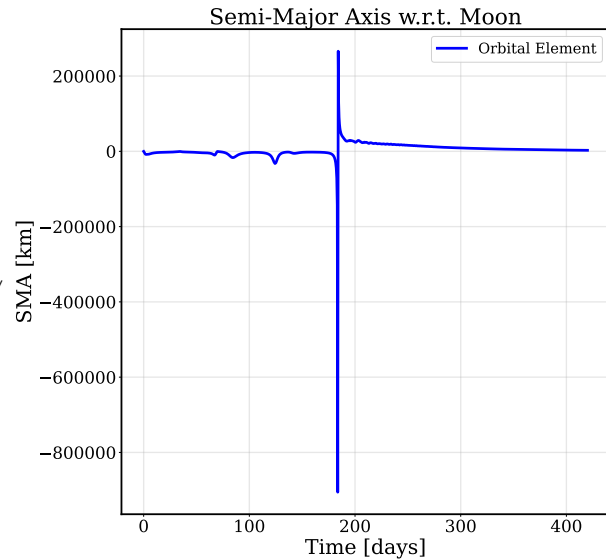


Fig. 10. Semi-major axis evolution w.r.t. Moon (full resolution). All parameters computed in MCI frame.

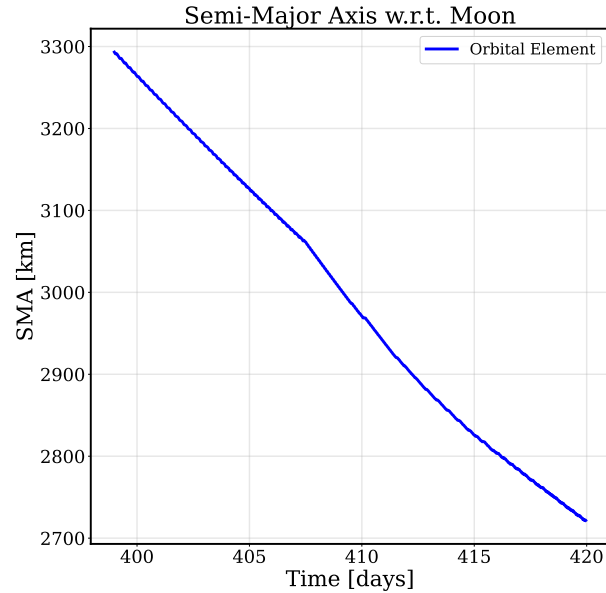


Fig. 11. Semi-major axis evolution w.r.t. Moon (last 10,000 points). All parameters computed in MCI frame.

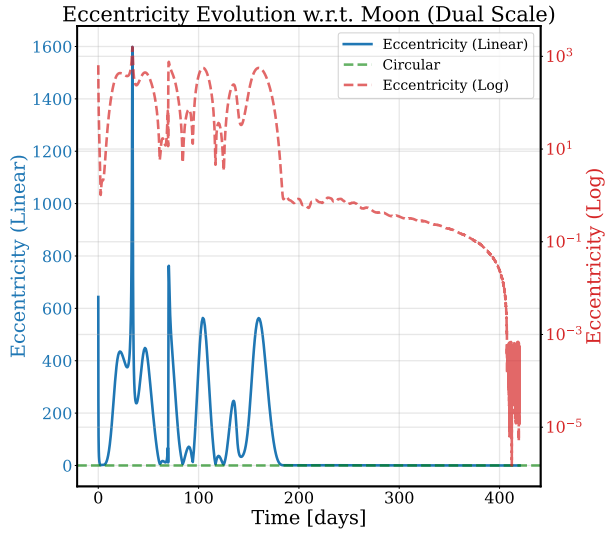


Fig. 12. Eccentricity evolution w.r.t. Moon (full resolution, dual-axis: linear left, logarithmic right). All parameters computed in MCI frame.

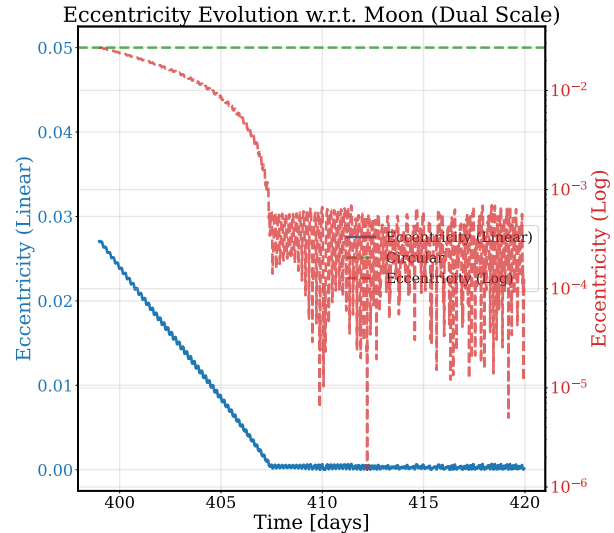


Fig. 14. Eccentricity evolution w.r.t. Moon (last 10,000 points, dual-axis: linear left, logarithmic right). All parameters computed in MCI frame.

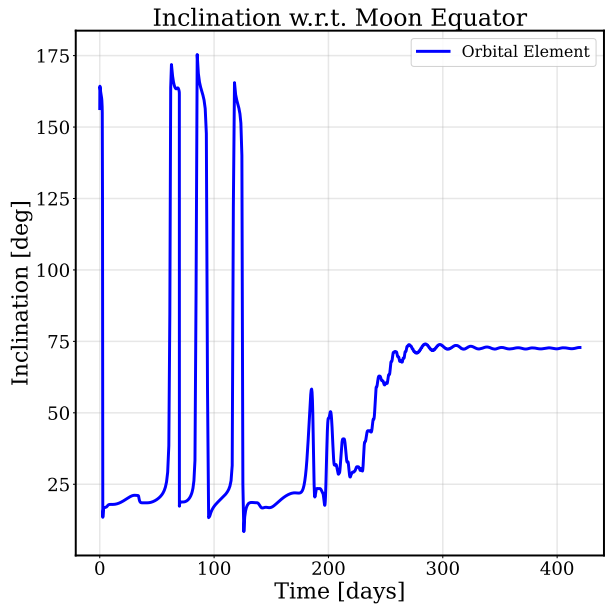


Fig. 13. Inclination w.r.t. Moon equator (full resolution). All parameters computed in MCI frame.

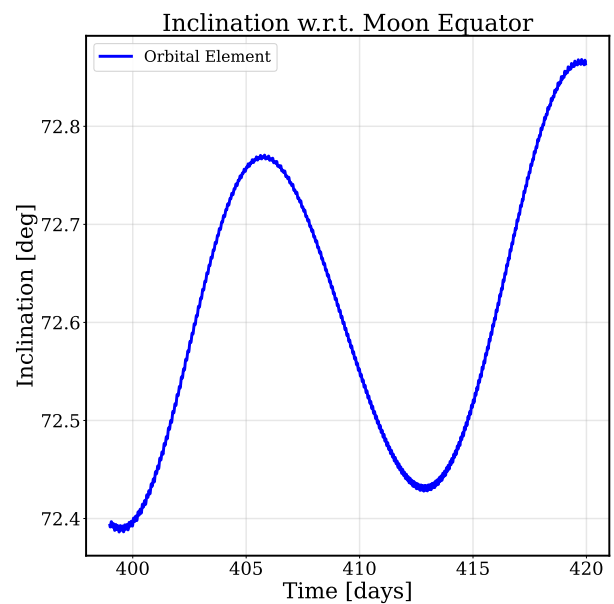


Fig. 15. Inclination w.r.t. Moon equator (last 10,000 points). All parameters computed in MCI frame.

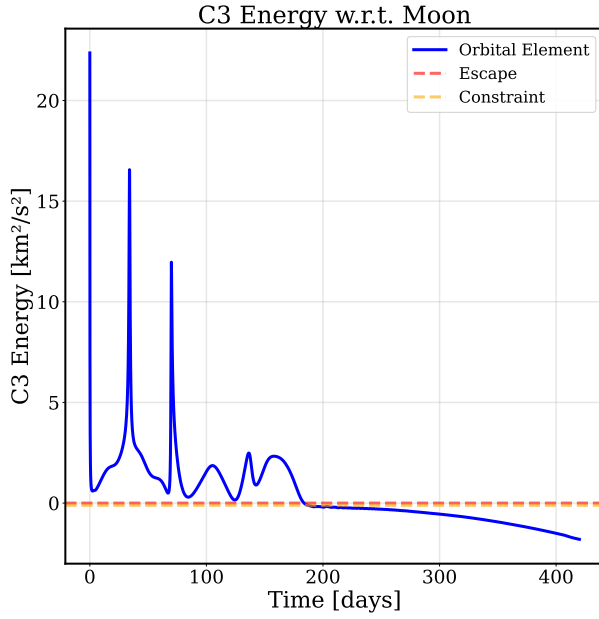


Fig. 16. C_3 energy evolution w.r.t. Moon (full resolution).
All parameters computed in MCI frame.

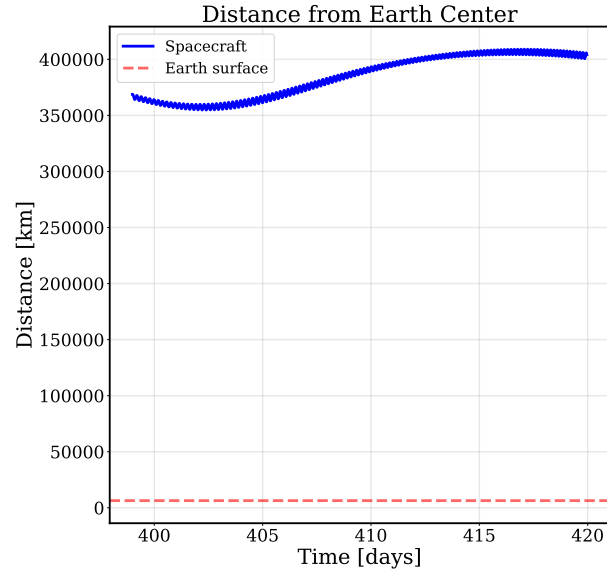


Fig. 18. Distance from Earth center (last 10,000 points).

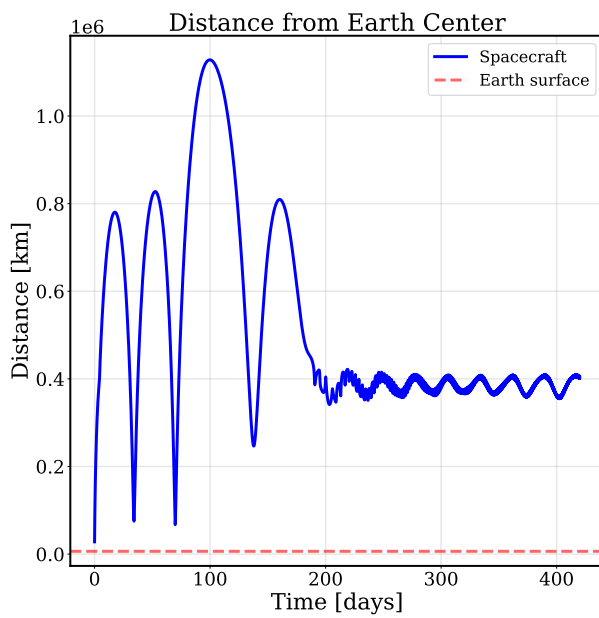


Fig. 17. Distance from Earth center (full resolution).

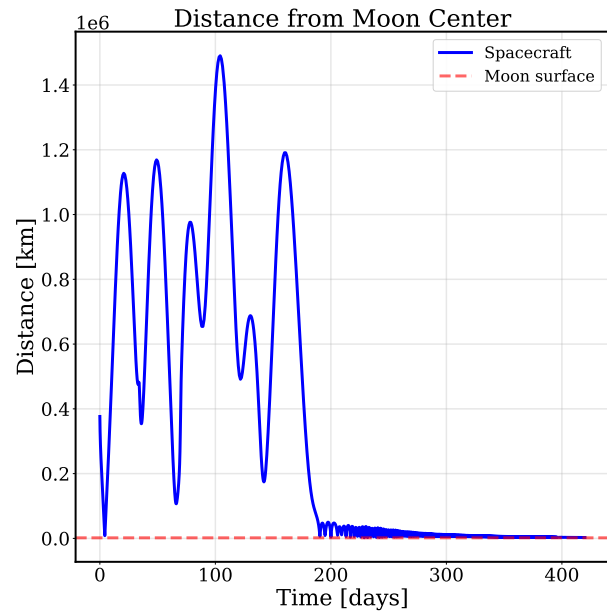


Fig. 19. Distance from Moon center (full resolution).